Journal of the Taiwan Institute of Chemical Engineers 45 (2014) 207–218

Contents lists available at SciVerse ScienceDirect

Journal of the Taiwan Institute of Chemical Engineers

journal homepage: www.elsevier.com/locate/jtice

# Hydrothermal synthesis of β-$ZnMoO_4$ crystals and their photocatalytic degradation of Victoria Blue R and phenol

Yu-Rou Jiang [a], Wenlian William Lee [b,c], Kung-Tung Chen [d], Ming-Chien Wang [a], Ken-Hao Chang [a], Chiing-Chang Chen [a,*]

[a] Department of Science Application and Dissemination, National Taichung University of Education, Taichung 40306, Taiwan, ROC
[b] Department of Occupational Safety and Health, Chung-Shan Medical University, Taichung 40201, Taiwan, ROC
[c] Department of Occupational Medicine, Chung Shan Medical University Hospital, Taichung 40201, Taiwan, ROC
[d] The Teaching Center of Natural Science, Minghsin University of Science and Technology, Hsinchu 30401, Taiwan, ROC

A R T I C L E I N F O

Article history:
Received 12 December 2012
Received in revised form 25 April 2013
Accepted 6 May 2013
Available online 6 June 2013

Keywords:
β-$ZnMoO_4$
Visible-light-responsive
Photocatalytic
Victoria Blue R
Phenol

A B S T R A C T

In this paper, the hydrothermal reaction with $Na_2MoO_4{\cdot}2H_2O$ and $Zn(NO_3)_2{\cdot}6H_2O$ as a precursor was investigated for the synthesis of β-$ZnMoO_4$ crystals. The β-$ZnMoO_4$ crystals were characterized by the X-ray diffraction (XRD), field emission scanning electronic microscopy–energy dispersive spectroscopy (FE-SEM–EDS), field emission transmission electronic microscopy–energy dispersive spectroscopy (FE-TEM–EDS), X-ray photoelectron (XPS), ultraviolet–visible (UV–vis), and Fourier transform infrared spectroscopy (FT-IR). Diffuse UV–vis spectra show that the β-$ZnMoO_4$ crystals have an indirect semiconductors with an optical bandgap of 2.48–2.69 eV. The photocatalytic efficiencies of powder suspensions were evaluated by measuring the Victoria Blue R (VBR) and phenol concentration. The as-prepared β-$ZnMoO_4$ crystals obtained at 280 °C for 24 h showed the best photocatalytic activity for VBR under UV irradiation and showed the best photocatalytic activity for VBR and phenol under visible-light irradiation. This is the first study to reveal excellent activities of β-$ZnMoO_4$ crystals are a promising visible-light-responsive photocatalyst.

## 1. Introduction

Over the past few decades, molybdenum has aroused ever increasing interest due to its potential applications in various fields, such as biology, photoluminescence, photocatalysis and its unexpectedly complex atomic arrangements [1,2]. Many studies have found that molybdates and tungstates are important materials in photoluminescence [3,4] and photocatalysis [5], and these have been successfully synthesized by different methods including hydrothermal processes [6,7], solid-state reaction methods [8], and precipitation/calcinations [9] and so on. The properties of the compounds depend greatly on its structure and morphology. In our other paper, square-plates $Bi_2WO_6$ showed the enhanced photoactivity for the decomposition of Crystal Violet [10]. $ZnMoO_4$ is an exceptionally important inorganic material with wide applications in catalysis [11], humidity sensors [12], battery materials [13], photoluminescence [2,14], anticorrosive paints [15] and photonic crystals [3] owing to its excellent optical and electrical performances and non-toxicity [16]. It is an inorganic material found in nature with two different types of crystalline phase: α-triclinic and β-monoclinic. In the α-$ZnMoO_4$ triclinic structure, all zinc atoms are bonded to six oxygen atoms, forming the distorted octahedral $[ZnO_6]$ clusters. The molybdenum atoms are coordinated to four oxygen atoms, resulting in the tetrahedral $[MoO_4]$ clusters [17]. On the other hand, the β-$ZnMoO_4$ monoclinic structure has both Zn and Mo atoms bonded to six oxygen atoms, which promote the origin of distorted octahedral $[ZnO_6]$/$[MoO_6]$ clusters, respectively [18].

Up to now, many efforts have been made in the study of properties and synthesis of $ZnMoO_4$ with nanometer-to-micrometer dimensions. However, these preparation routes require high temperatures, long processing times and use of organic precursors/solvents. Recently, the hydrothermal methods have been well-employed in the preparation, growth and morphological control of different oxide materials [19–23]. In particular, the main advantage of the hydrothermal is the ability to obtain pure oxides at low temperature conditions (<300 °C). Moreover, capping agents, templates and/or surfactants can be added in the chemical solution to be submitted to the hydrothermal treatment in order to control the crystal shapes and sizes (nano-, meso- or micro-scale) [2,24,25].

---

[*] Corresponding author. Tel.: +886 4 2218 3406; fax: +886 4 2218 3560.
E-mail addresses: ccchen@mail.ntcu.edu.tw, ccchen@ms3.ntcu.edu.tw (C.-C. Chen).

1876-1070/$ – see front matter © 2013 Taiwan Institute of Chemical Engineers. Published by Elsevier B.V. All rights reserved.
http://dx.doi.org/10.1016/j.jtice.2013.05.007

Dyes are an important group of chemical environmental pollution, and they are usually released in the industrial wastes, consequently, discharged to the surface waters. The dyes may inhibit sunlight into rivers and affect the photosynthetic reactions [26,27]. The dyes even affect aquatic life and food chain. In order to protect the environment, there are many new research methods in waste water treatment. The photocatalysis process has been successfully used to degrade pollutants during the past few decades [28,29]. In recent years, there is an important issue with different process technologies or different starting materials to produce a better photocatalytic efficiency of the photocatalyst [1].

Therefore, in this paper, hydrothermal reaction with $Zn(NO_3)_2{\cdot}6H_2O$ and $Na_2MoO_4{\cdot}2H_2O$ as a precursor was investigated for the synthesis of $ZnMoO_4$ without surfactant on the growth process. Moreover, to obtain excellent activities of β-$ZnMoO_4$ crystals are a promising visible-light-responsive photocatalyst.

## 2. Experimental details

### 2.1. Materials and preparation of photocatalysts

Using 4 mmol $Zn(NO_3)_2{\cdot}6H_2O$ and 2 mmol $Na_2MoO_4{\cdot}2H_2O$ as the start materials, β-$ZnMoO_4$ powders could be synthesized by hydrothermal reaction. The start materials were mixed together and 10 mL distilled water was added. These solutions were simultaneously mixed inside a stainless autoclave and then kept under constant stirring. The mixture was transferred to a Teflon-lined autoclave (capacity: 23 mL) and the resulting precursors were used as heated at 180 °C (or 230, 280 °C) for 6 h (or 12, 24, 48, 72 h).

Completed the hydrothermal processing, the stainless autoclave was naturally cooled to room temperature. The precipitates were filtered off, washed several times with distilled water to remove the residual ions, and dried at 60 °C for 24 h. A variety of reaction conditions were employed (including various reaction temperature and times) as shown in Table 1, namely ZM-180-4 to ZM-280-24 for β-$ZnMoO_4$ samples, respectively. The as-prepared samples were characterized by XRD, FE-SEM–EDS, FE-TEM, HRXPS, DRS, and FT-IR. These experimental conditions were favorable to promote the stoichiometric reactions between the $Zn^{2+}$ and $MoO_4^{2-}$ ions, which are responsible for the formation of the crystalline β-$ZnMoO_4$ microcrystals, as shown in Eqs. (1)–(3):

$$Na_2MoO_4{\cdot}2H_2O_{(s)} \rightarrow 2Na^+{}_{(aq)} + MoO_4^{2-}{}_{(aq)} + 2H_2O \quad (1)$$

$$Zn(NO_3)_2{\cdot}6H_2O_{(s)} \rightarrow Zn^{2+}{}_{(aq)} + 2NO_3^-{}_{(aq)} + 6H_2O \quad (2)$$

$$MoO_4^{2-}{}_{(aq)} + Zn^{2+}{}_{(aq)} \rightarrow \beta\text{-}ZnMoO_{4(s)} \quad (3)$$

**Table 1**
Physical properties of β-$ZnMoO_4$.

| Catalyst code | Temperature (°C) | Time (h) | EDS of atomic ratio (%) | | | $E_g$ (eV) |
|---|---|---|---|---|---|---|
| | | | Zn | Mo | O | |
| ZM-180-24 | 180 | 24 | 12.43 | 12.02 | 75.55 | 2.66 |
| ZM-180-48 | 180 | 48 | 11.46 | 11.91 | 76.63 | 2.63 |
| ZM-180-72 | 180 | 72 | 11.43 | 11.94 | 76.63 | 2.59 |
| ZM-230-12 | 230 | 12 | 12.24 | 12.27 | 75.49 | 2.48 |
| ZM-230-24 | 230 | 24 | 12.07 | 12.19 | 75.74 | 2.63 |
| ZM-230-48 | 230 | 48 | 12.31 | 12.60 | 75.09 | 2.68 |
| ZM-280-12 | 280 | 12 | 11.14 | 11.11 | 77.75 | 2.64 |
| ZM-280-24 | 280 | 24 | 11.59 | 11.24 | 77.17 | 2.69 |

### 2.2. Instruments and characterization

The prepared catalysts were checked with both energy dispersive spectroscopy (EDS) and high resolution X-ray photoelectron spectrometer (HR-XPS). X-ray powder diffraction (XRD) patterns were recorded on a MAC Sience, MXP18 X-ray diffractometer with Cu Kα radiation, operated at 40 kV and 80 mA. An HRXPS measurement was carried out with ULVAC-PHI XPS. The Al Kα radiation was generated with a voltage of 15 kV. Field emission scanning electron microscopy (FE-SEM) measurement was carried out with a field-emission microscope (JEOL JSM-7401F) at an acceleration voltage of 15 kV. The field-emission transmission electron microscopy (FE-TEM) images, SAED pattern, high-resolution transmission electron microscopy (HRTEM) images and an energy-dispersive X-ray spectrum (EDS) were taken on a JEOL-2010 transmission electron microscope with an accelerating voltage of 200 kV. At the liquid nitrogen temperature, the BET specific surface areas of the samples were measured with an automatic system (Micromeritics Gemini 2370C) with nitrogen gas as the adsorbate. Fourier transform infrared (FT-IR) spectra were collected on a Nicolet 380 FT-IR spectrometer. UV–vis diffuse reflectance spectra were recorded on a Scinco SA-13.1 spectrophotometer at room temperature.

Waters ZQ LC/MS system, equipped with a binary pump, a photodiode array detector, an autosampler, and a micromass detector, was used for separation and identification. After each irradiation cycle, the amount of the residual dye was determined by HPLC. The analysis of organic intermediates was accomplished by HPLC–ESI-MS after the readjustment of the chromatographic conditions in order to make the mobile phase compatible with the working conditions of the mass spectrometer. Two different kinds of solvents were prepared in this study. Solvent A was 25 mM aqueous ammonium acetate buffer (pH 6.9) while solvent B was methanol instead of ammonium acetate. LC was carried out on an Atlantis$^{TM}$ dC18 column (250 mm × 4.6 mm i.d., dp = 5 μm). The flow rate of the mobile phase was set at 1.0 mL/min. A linear gradient was set as follows: $t = 0, A = 95, B = 5$; $t = 20, A = 50, B = 50$; $t = 60, A = 10, B = 90$; $t = 65, A = 95, B = 5$. The column effluent was introduced into the ESI source of the mass spectrometer.

Equipped with an ESI interface, the quadruple mass spectrometer with heated nebulizer probe at 200 °C was used with an ion source temperature of 120 °C. ESI was carried out with the vaporizer at 200 °C and nitrogen as sheath (551 kPa) and auxiliary (138 kPa) gas to assist with the preliminary nebulization and to initiate the ionization process. A discharge current of 5 μA was applied. Cone lens and capillary voltages were optimized for the maximum response during perfusion of the VBR standard.

### 2.3. Procedure and analysis

Aqueous suspensions of VBR (100 mL, 50 ppm) and the amounts of catalyst powders were placed in the Pyrex flask. The pH value of the suspensions was adjusted by adding either NaOH or $HNO_3$ solutions. Prior to irradiation, the suspensions were magnetically stirred in the dark for *ca.* 30 min to establish adsorption/desorption equilibrium between the dye, and the surface of the catalyst under ambient air-equilibrated conditions. Irradiations were carried out using two UV-365 nm (15 W) or visible-light lamps (300 W Xe arc). Under UV irradiation, an average irradiation intensity of 5.2 W/m$^2$ was maintained throughout the experiments and was measured by internal radiometer. Under visible-light irradiation, the reactor was then irradiated by a 300 W Xe arc lamp. The light intensity was fixed on 435.1 W/m$^2$ when the reactor was placed 15 cm away from the light's source. Irradiation experiments of VBR were carried out on stirred aqueous solution contained in a 100 mL flask. At given time intervals, 5 mL aliquots were sampled and centrifuged to remove the particles. The filtrates were analyzed by HPLC–PDA–ESI-MS.

## 3. Results and discussion

### 3.1. Characterization of the photocatalysts

As it was shown in Fig. 1, the influence of reactive temperature and time on the formation of β-$ZnMoO_4$ crystalline phase was also studied by XRD. These peaks are indexed to crystalline structure of β-$ZnMoO_4$ (JCPDS card no. 25-1024), corresponding to the indices of crystalline planes respectively [5]. The similar features and intensities are found in all samples, indicating that under the reaction condition the hydrothermal reaction can obtain good quality crystal in the range of treating temperature and time. No diffraction peaks for the other crystallites were obviously detected.

From the FE-SEM images, it can be seen that the morphology of the β-$ZnMoO_4$ sample obtained at the longer reaction time shows an irregular plate-like crystals to irregular corner crystals (Fig. 2) and at the higher temperature shows a formation of the larger corner crystals (Fig. 3). The crystal particle size of the sample has a wide range from 2 to 10 μm. This growth mechanism was based on the FE-SEM micrographs. A possible growth mechanism for the microcrystals was proposed to explain in details the effect of time and temperature on the shape and size (Fig. 4). Firstly in Fig. 4, the free energy of solvation related to the $H_2O$ molecules causes a fast dissociation of the chemical salts in solution, so that the $Zn^{2+}$ and $MoO_4{}^{2-}$ ions are rapidly solvated by these molecules. The partial negative charges belonging to the $H_2O$ molecules electrostatically attract the $Zn^{2+}$ ions, while its partial positive charges interact with the $MoO_4{}^{2-}$ ions [30]. In principle, during the hydrothermal processing performed at 180 °C for 24, 48,72 h inside the stainless autoclave, this closed environment provided the thermodynamic conditions to break the aqueous solvation shell, favoring the electrostatic attraction and between both the $Zn^{2+}$ and $MoO_4{}^{2-}$ ions by the nucleation process with the formation of first β-$ZnMoO_{4(s)}$ precipitates or nuclei (Fig. 4a). When the $H_2O$ molecules were used as solvent, the hydrogen bonds (highly polar) were able to make two hydrogen atoms ($H^{\delta+}$), belonging to one $H_2O$ molecule, strongly interact with other two neighboring $H_2O$ molecules. In another case also involving the $H_2O$ solution, the oxygen atoms ($O^{\delta-}$) (containing two free electron pairs) of each $H_2O$ molecule have the ability of form the hydrogen bridges or interact with the H atoms bonded to other $H_2O$ molecules. There are a correct number of hydrogen atoms ($H^{\delta+}$) and lone electron pairs within the liquid system, so that each them can be involved by hydrogen bonds [31]. After formation of the first nuclei, the hydrothermal conditions intensify the effective collision frequency involving the anisotropic nanoparticles in suspension, producing a mutual aggregation between them. This self-assembly process can occur in a spontaneous way and/or and hydrothermal conditions, where several nanocrystals are aggregated in a same or different crystallographic plane which can drive the growth of oriented aggregate, meso- and nanocrystals [32]. Theoretically after an effective chock, if the nanoparticles share a common crystallographic orientation, they may remain irreversibly attached [33]. Moreover, the nanoparticles can be surrounded by $H_2O$ molecules in this suspension, which tend to change or direct the growth of the microcrystals. After agglomeration process (disordered assemblies), probably occurred the coalescence of nanoparticles followed by Ostwald ripening [2,34], resulting in the irregular plate-like β-$ZnMoO_4$ microcrystals. From Table 2, the EDS results showed that the main elements of these samples were molybdenum, zinc, and oxygen. The Zn/Mo atomic ratio of the samples was within the range of 0.96–1.03, which corresponded to 3–4% excess of Zn or Mo compared to the stoichiometric ratio (Zn:Mo = 1:1). The excessive carbon in the examined catalysts was possibly due to the organic contaminant.

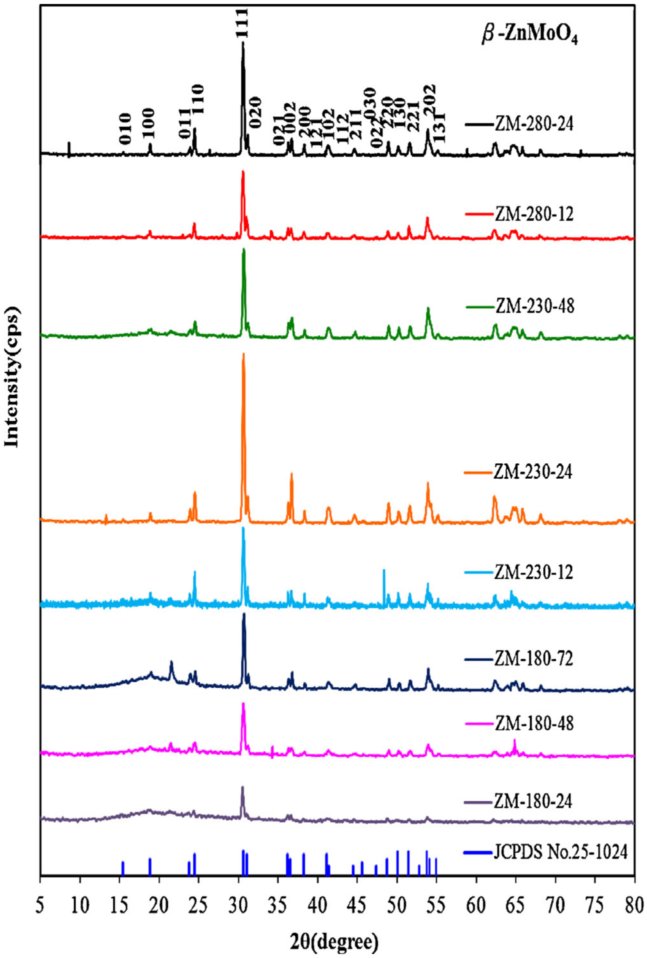

**Fig. 1.** XRD patterns of β-$ZnMoO_4$ crystals.

Fig. 5a and b is a TEM and HRTEM images of an individual β-$ZnMoO_4$ crystals. The ED pattern can be indexed to the diffraction pattern of [1 0 0] zone axis. An HRTEM image of an individual β-$ZnMoO_4$ crystals shown in Fig. 5a presents the lattice spacings are about 0.491 nm, corresponding to the lattice spacings of the (1 0 0) planes for β-$ZnMoO_4$ crystals. In Fig. 5c is the corresponding SAED pattern recorded from the irregular plate-like crystals side. These pattern spots demonstrate the poly-crystal nature of β-$ZnMoO_4$ crystals. The bright spots shown in the SAED pattern could be indexed to (1 0 0) and (1 3 0) of tetragonal phase β-$ZnMoO_4$. These results are in well accordance with that of XRD pattern in Fig. 1. In Fig. 5d is an EDS, only Zn, Mo, and O peaks observed, indicating that the product is composed of Zn, Mo, and O. Quantitative EDS analysis shows that the atom ratio of Zn/Mo is 1:1.3.

The characteristic binding energy value of 231.73–231.79 eV for Mo $3d_{5/2}$ revealed a hexavalent oxidation state for molybdenum and without obvious displacement [6] and 1020.89–1021.27 eV for Zn $2p_{3/2}$ revealed a bivalent oxidation state for zinc is shown in Fig. 6. It can be seen that three materials are composed of particles in Table 2. The Zn/Mo atomic ratio of the samples was within the range of 0.78–1.28, which corresponded to 22–28% excess of Zn or Mo compared to the stoichiometric ratio (Zn:Mo = 1:1).

Fig. 7 shows the FT-IR spectra produced under different synthesis temperatures. Those at 956 $cm^{-1}$ were specified as the $\nu_1$ stretching of Mo–O in bridging Mo–O–Mo linkages. The vibrations at 869 $cm^{-1}$ corresponded to the $\nu_1$ stretching of

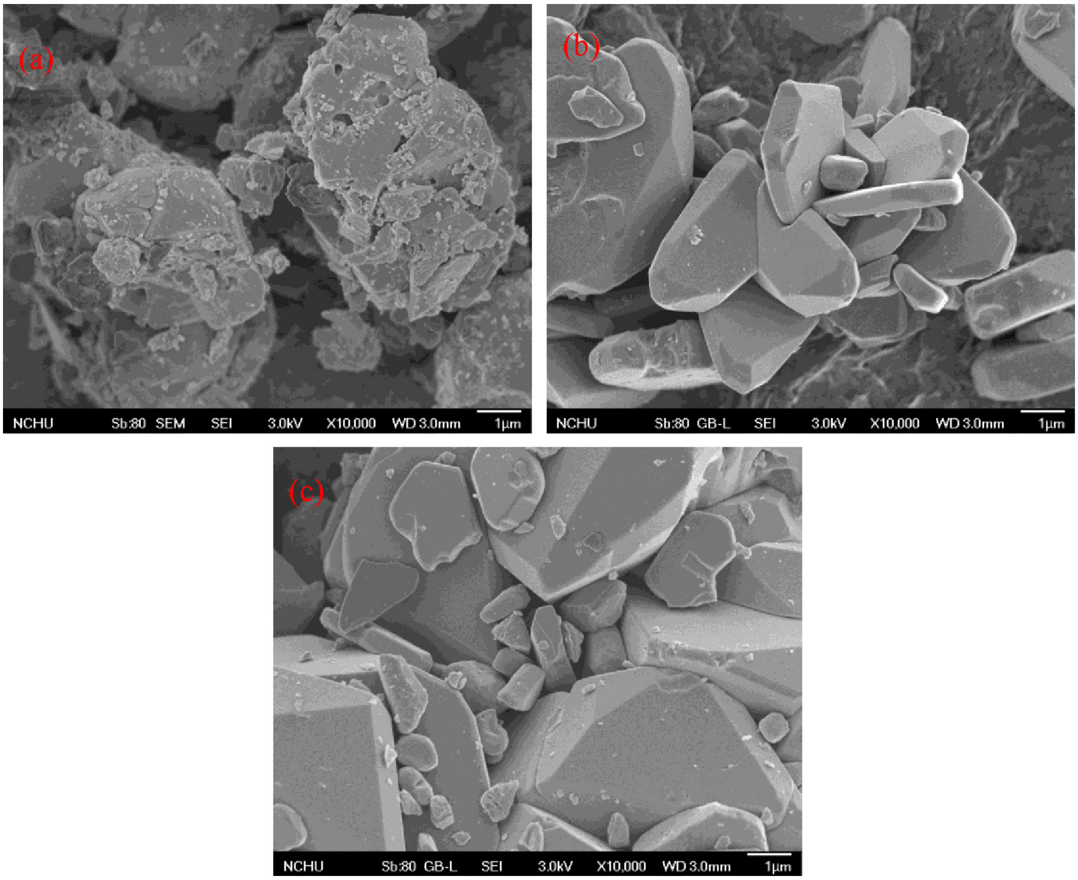

**Fig. 2.** SEM images of the β-$ZnMoO_4$ crystals. (a) Temp. = 180 °C, time = 24 h; (b) Temp. = 180 °C, time = 48 h; (c) Temp. = 180 °C, time = 72 h.

$(MoO_6)^{2-}$ octahedrons, and those at 756 $cm^{-1}$ to the $\nu_3$ stretching of Mo–O [35,36]. The infrared spectrum shows the characteristic doublet absorption due to 850, 760 and 520 $cm^{-1}$ (Zn–O vibrational modes), respectively. The observed behavior can be associated with the energy difference between the valence band and conduction band for this material.

UV–visible measurements of all the samples are shown in Fig. 8 and Table 1. UV–visible absorption of the three samples indicated an exponential decreasing of the photonic absorbance ($\alpha$) attenuated through the product. Its indirect $E_g$ was determined (by extrapolating the linear portion of the curve to zero absorption) to be 2.74–2.85 eV – very close to that for $xMoO_3-(1-x)ZnO$ [30], but less than that estimated for perfect $ZnMoO_4$ [37].

### 3.2. Photocatalytic activities

The photodegradation rate of the VBR was found to decrease with the increase of reaction time (Fig. 9). The adsorption resulted in a decrease of about 9.5%, 15.1%, and 9.8% in the VBR concentration after 36 h, and a decrease in the photocatalytic efficiencies of 89.2%, 81.6%, and 99.1% under visible light irradiation after 84 h and 97.5%, 99.3%, and 52.8% under UV light irradiation after 24 h in the VBR concentration being decolorized for 180 °C, 230 °C, 280 °C, respectively.

The photodegradation rate of the phenol was found to decrease with the increase of reaction time (Fig. 10). The adsorption resulted in a decrease of about 5.1%, 5.1%, and 5.2% in the phenol concentration after 96 h, and a decrease in the photocatalytic efficiencies of 60.5%, 57.2%, and 88.6% under visible light irradiation in the phenol concentration being decomposed after 96 h for 180 °C, 230 °C, 280 °C, respectively.

### 3.3. Separation and identification of the intermediates

To obtain a better understanding of the mechanistic details of these β-$ZnMoO_4$-assisted photodegradation of the VBR dye with UV or visible light irradiation, a large number of intermediates of the process were separated, identified, and characterized by a HPLC–PDA–ESI-MS. The chromatograms were obtained for an irradiated VBR solution after 36 h, at pH 9, with UV light in the presence of β-$ZnMoO_4$ (0.5 g/L). These chromatograms, recorded at 580 nm, 350 nm, and 300 nm, are illustrated in Fig. 11. With irradiation up to 36 h, twenty components are identified, all with the retention times of less than 65 min. Several categories of intermediates can be distinguished in Fig. 11. We denoted the VBR dye and its related intermediates as species A–K, a–e, l–p, α–γ, and δ–ε. The maximum absorption band of each intermediate in the visible and ultraviolet spectral region was measured, and these bands correspond to the peaks in Table 3, respectively. The intermediates were further identified using the HPLC–ESI mass spectrometric method and are illustrated in Table 3. The molecular ion peaks appeared to be in the acid forms of the intermediates. The concentration of the other intermediates may be under the detection limit.

The first groups were signed in the chromatogram and are illustrated in Fig. 11, recorded at 580 nm. From the results of mass spectral analysis, we confirmed that the component A, $m/z = 422.2$, in the liquid chromatogram is VBR; the other components are B, $m/z = 408.2$; C, $m/z = 394.2$; D, $m/z = 394.3$; E, $m/z = 394.2$; F, $m/z = 380.2$; G, $m/z = 380.2$; H, $m/z = 366.2$; I, $m/z = 366.2$; J, $m/z = 366.3$. The intermediates have the wavelength position of their major absorption bands moved toward the blue region, $\lambda_{max}$, A, 619.2 nm; B, 609.4 nm; C, 600.8 nm; D, 598.0 nm; E, 609.4 nm; F,

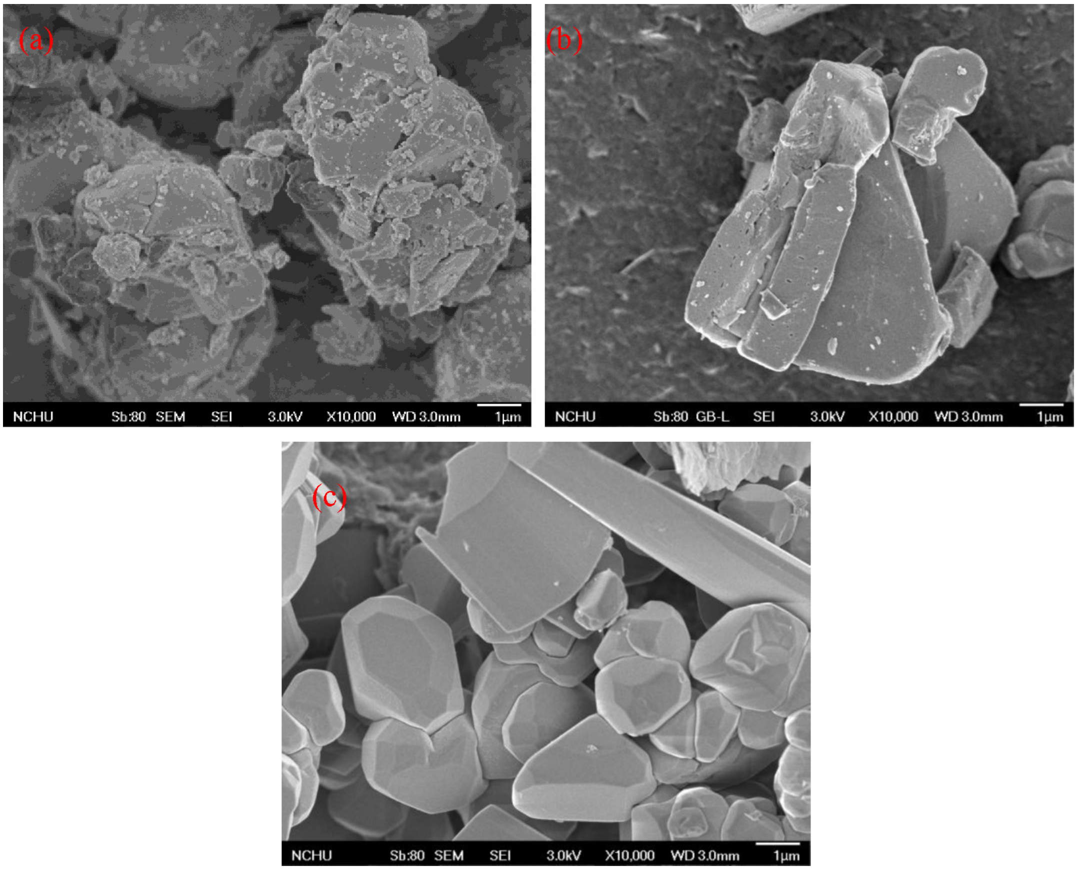

**Fig. 3.** SEM images of the β-$ZnMoO_4$ crystals. (a) Temp. = 180 °C, time = 24 h; (b) Temp. = 230 °C, time = 24 h; (c) Temp. = 280 °C, time = 24 h.

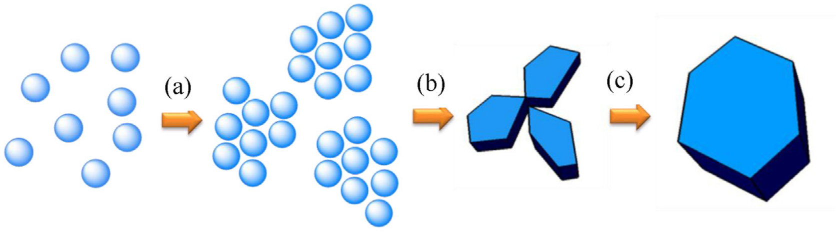

**Fig. 4.** Schematic illustration of the main stages involved in the growth mechanism of β-$ZnMoO_4$ crystals synthesized in hydrothermal system at 180 °C: (a) nucleation and origin of the first clusters or nuclei; (b) self-assembly process of small crystals; (c) crystal growth process.

591.0 nm; G, 605.7 nm; H, 589.8 nm; I, 564.1 nm; J, 560.4 nm; K, 566.5 nm. The first group of intermediates may represent the *N*-de-alkylation of the VBR dye.

The second groups were marked in the chromatogram and are illustrated in Fig. 11, recorded at 350 nm. Mass spectral analysis confirmed the components to be: a, $m/z = 269.1$; b, $m/z = 255.1$; c, $m/z = 241.1$; d, $m/z = 241.0$; e, $m/z = 227.1$. The concentration of the other intermediates may have been under the detection limit. The maximum absorption band of each intermediate in the ultraviolet spectral region around 350 nm is displayed in Table 3, and they correspond to the peaks a–f in Fig. 11. The a–e intermediates, produced by the stepwise cleavage of the VBR derivatives of the chromophore ring structure or the *N*-de-ethylated a, have the wavelength position of their major absorption bands moved toward the blue region, $\lambda_{max}$, a, 363.9 nm; b, 355.8 nm; c, 362.9 nm; d, 360.9 nm; e, 353.4 nm. The proposed intermediate (a) has been compared with standard material of 4-(*N*,*N*-dimethylamino)-4′-(*N*′,*N*′-dimethylamino) benzophenone. The retention times and absorption spectra are identical. The intermediates identified in this study were also identified in a previous study [38].

**Table 2**
Physical properties of β-$ZnMoO_4$.

| Catalyst code | XPS of atomic ratio (%) | | |
|---|---|---|---|
| | Zn | Mo | O |
| ZM-180-24 | 13.1 | 16.9 | 70.0 |
| ZM-230-24 | 13.3 | 16.8 | 69.9 |
| ZM-280-24 | 14.8 | 11.6 | 73.6 |

### *3.4. Proposed mechanism of VBR degradation*

According to the literature [39,40], the low recombination rate between photogenerated electrons and holes on the crystal surface is the key factor for a good photocatalytic property. Thus, the holes ($h^+$) generated by the distorted [$SrO_8$] and [$WO_4$] clusters or can provide favorable conditions for the electron ($e^-$)–hole ($h^+$) recombination events. This phenomenon is caused by the existence of distorted $[WO_4]_d/[SrO_8]_d$ clusters (intrinsic defects)

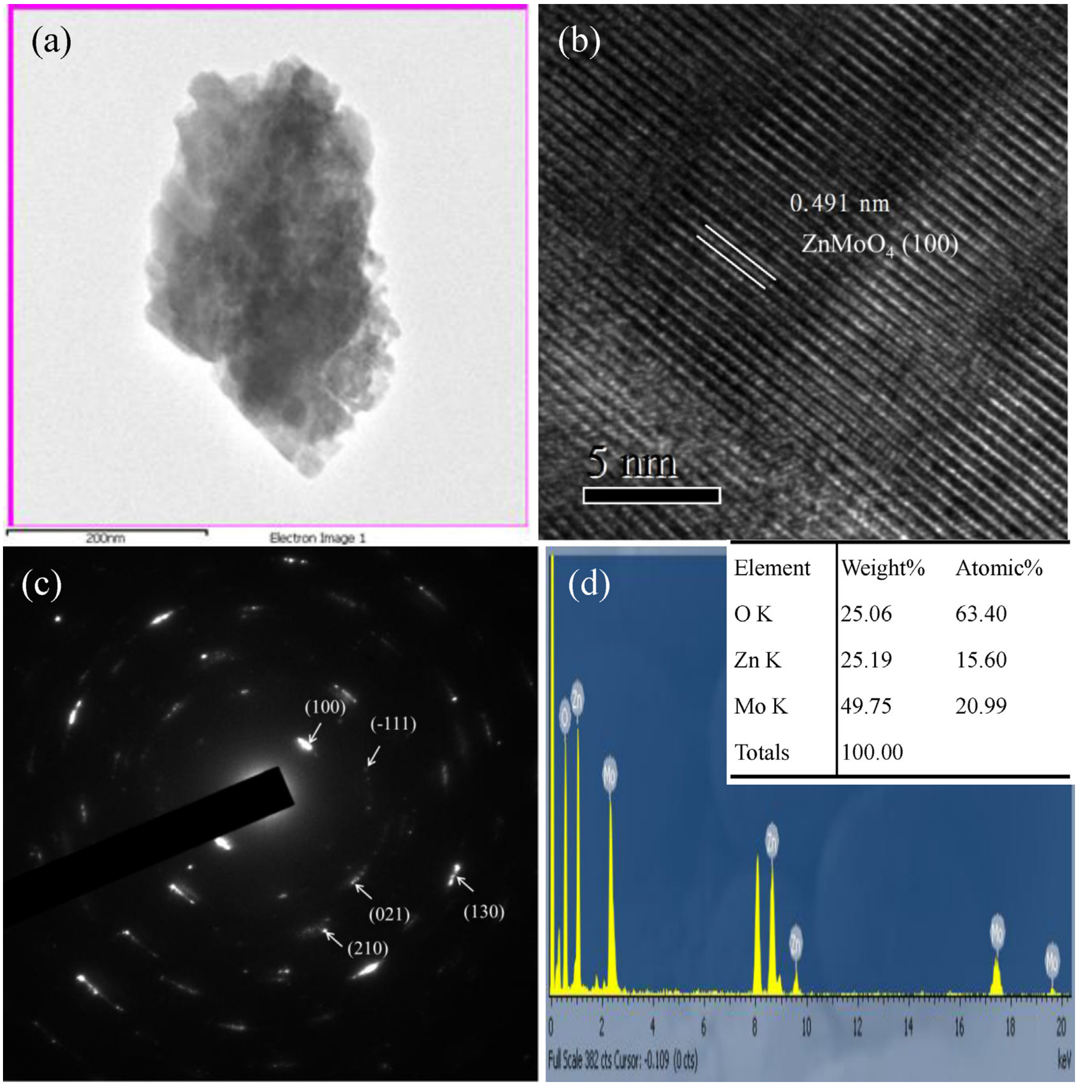

| Element | Weight% | Atomic% |
|---|---|---|
| O K | 25.06 | 63.40 |
| Zn K | 25.19 | 15.60 |
| Mo K | 49.75 | 20.99 |
| Totals | 100.00 | |

**Fig. 5.** (a) TEM and (b) HRTEM images, (c) SAED pattern, and (d) EDS of β-$ZnMoO_4$ crystal obtained in hydrothermal system at 180 °C for 24 h.

into the Scheelite-type tetragonal structure. These defects are able to polarize the lattice and lead to the electronic transitions between $[WO_4]_d{}^x/[SrO_8]_d{}^x$ (disordered clusters) and $[WO_4]_o{}^x/[SrO_8]_o{}^x$ (ordered clusters).

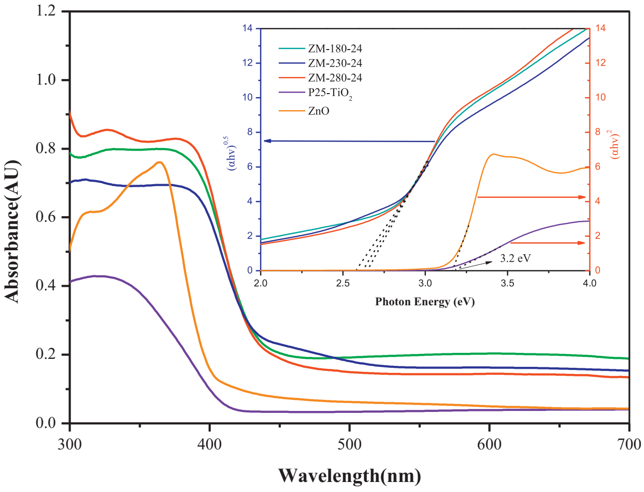

**Fig. 6.** XPS spectra of β-$ZnMoO_4$ crystals, W 4f, Zn 2p, and O 1s.

The β-$ZnMoO_4$ monoclinic structure has both Zn and Mo atoms bonded to six oxygen atoms, which promote the origin of distorted octahedral $[ZnO_6]/[MoO_6]$ clusters, respectively [18]. In this study, a model based on complex clusters [39,40] was proposed to

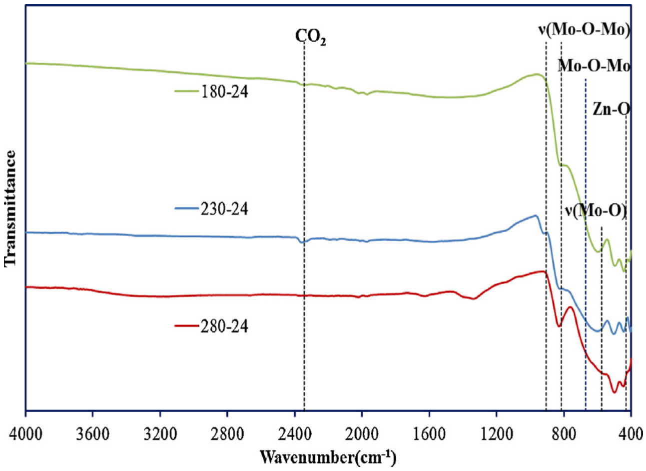

**Fig. 7.** FT-IR spectra of β-$ZnMoO_4$ crystals prepared using hydrothermal treatment with various synthesis temperatures: 180 °C, 230 °C, and 280 °C.

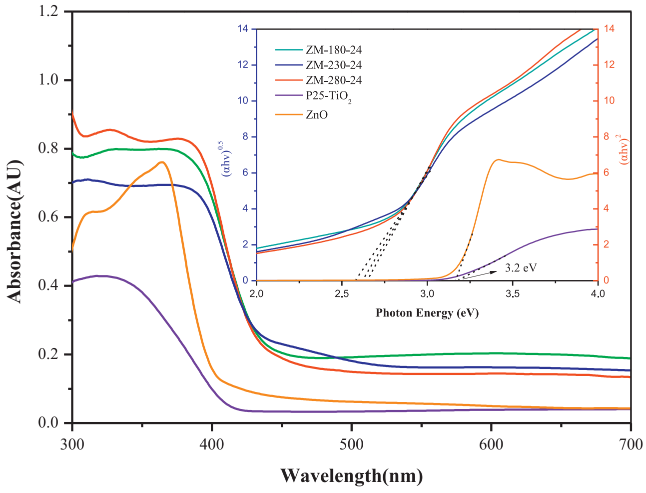

**Fig. 8.** UV–vis diffuse reflectance spectra of β-$ZnMoO_4$ crystals prepared using hydrothermal method with various temperatures.

explain the photocatalytic activity of β-$ZnMoO_4$ crystals due to the photo-oxidation of CV and phenol. Initially, we assume that before the UV excitation light excitation reaches the system, the β-$ZnMoO_4$ catalyst has the ability to generate pairs ($e^-$–$h^+$). This characteristic is due to intrinsic defects in the lattice of materials with octahedral structures. Therefore, these defects which are caused by distorted $[MoO_6]_d$ clusters can polarize in the lattice and lead to possible electronic transitions between disordered $[MoO_6]_d^{x}$ and ordered $[MoO_6]_o^{x}$ clusters. When the UV light is absorbed by the crystals, the following processes can occur as expressed in Eqs. (4)–(7):

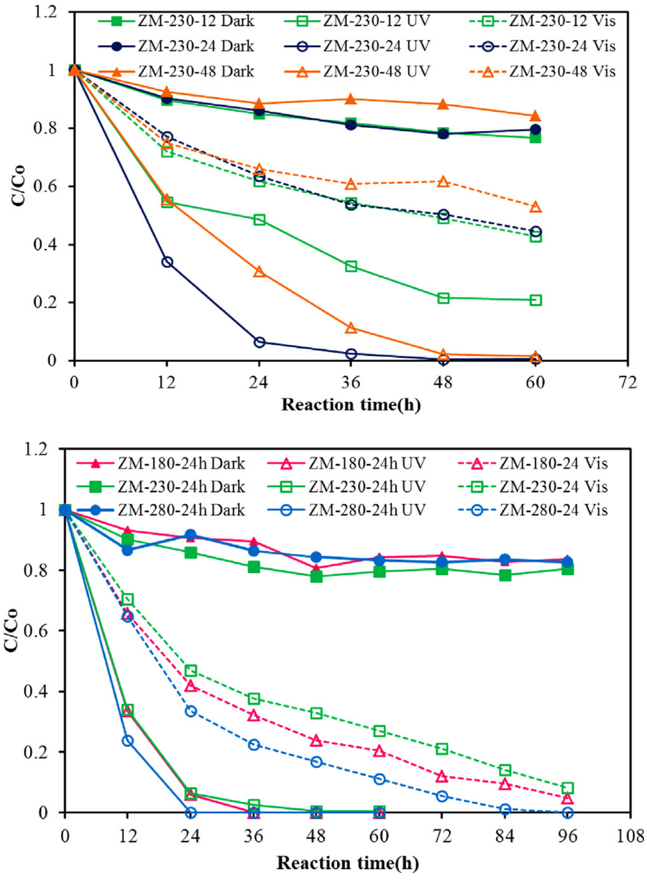

**Fig. 9.** The photocatalytic activity of β-$ZnMoO_4$ crystals for VBR under UV or visible-light irradiation. (0.01 g/L VBR; 0.05 g/L β-$ZnMoO_4$).

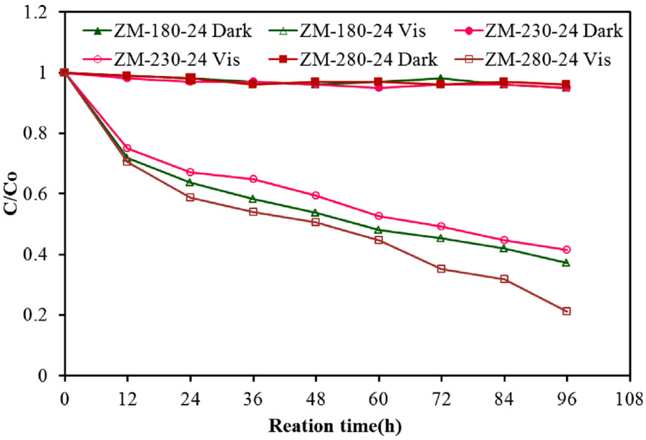

**Fig. 10.** The photocatalytic activity of β-$ZnMoO_4$ crystals under visible-light irradiation (0.01 g/L phenol; 0.05 g/L β-$ZnMoO_4$).

$$ZnMoO_{6(defects)} + h\nu \rightarrow [MoO_6]_d^{x} + [MoO_6]_o^{x} \quad (4)$$

$$[MoO_6]_d^{x} + [MoO_6]_o^{x} + h\nu \rightarrow [MoO_6]_d^{\bullet} + [MoO_6]_o^{\prime} \quad (5)$$

$$ZnMoO_{6(defects)} + h\nu \rightarrow [ZnO_6]_d^{x} + [ZnO_6]_o^{x} \quad (6)$$

$$[ZnO_6]_d^{x} + [ZnO_6]_o^{x} + h\nu \rightarrow [ZnO_6]_d^{\bullet} + [ZnO_6]_o^{\prime} \quad (7)$$

where $[MoO_6]_d^{\bullet}$ (or $[ZnO_6]_d^{\bullet}$) clusters are located in intermediate levels (VC) near the VB while the $[MoO_6]_o^{\prime}$ (or $[ZnO_6]_o^{\prime}$) clusters are located in intermediate levels (BC) below the CB. Moreover, the CV or phenol is also excited by UV light as shown in Eq. (8):

$$CV\ (\text{or phenol}) + h\nu \rightarrow CV^{*}\ (\text{or phenol}^{*}) \quad (8)$$

In the following step, due to an intermediary energy level between the VC and the BC of these crystals, electrons near them can be excited when illuminated by UV-light. This UV light energy can promote these excited electrons from the VB to the CB of the crystals. This process leads the formation of pairs ($e^-$–$h^+$) within the crystal band gap. During photooxidation processes, the species generated $[MoO_6]_d^{\bullet}$ or $[ZnO_6]_d^{\bullet}$ cluster can interact with the CV* and $H_2O$ molecules [41,42] as shown in Eqs. (9)–(12), which is a possible process that occurs in the VB:

$$[MoO_6]_d^{\bullet} \cdots CV^{*}_{ads} + h\nu \rightarrow [MoO_6]_d^{x} + CV^{\bullet} \quad (9)$$

$$[MoO_6]_d^{\bullet} \cdots H_2O^{*}_{ads} + h\nu \rightarrow [MoO_6]_d^{x} + OH^{\bullet} + H^{*} \quad (10)$$

$$[ZnO_6]_d^{\bullet} \cdots CV^{*}_{ads} + h\nu \rightarrow [ZnO_6]_d^{x} + CV^{\bullet} \quad (11)$$

$$[ZnO_6]_d^{\bullet} \cdots H_2O^{*}_{ads} + h\nu \rightarrow [ZnO_6]_d^{x} + OH^{\bullet} + H^{*} \quad (12)$$

On the other hand, the $[MoO_6]_d^{\bullet}$ (or $[ZnO_6]_d^{\bullet}$) clusters can react with the $H^*$ to generate ($H^+$) while, the species generated $[MoO_6]_o^{\prime}$ (or $[ZnO_6]_o^{\prime}$) clusters react with oxygen molecules in an aqueous solution [39,40,43], as shown in Eqs. (13) and (14), which is a possible process that occurs in the CB:

$$[MoO_6]_o^{\prime} + O_2 + h\nu \rightarrow [MoO_6]_o^{x} + O_2^{\bullet -} \quad (13)$$

$$[ZnO_6]_o^{\prime} + O_2 + h\nu \rightarrow [ZnO_6]_o^{x} + O_2^{\bullet -} \quad (14)$$

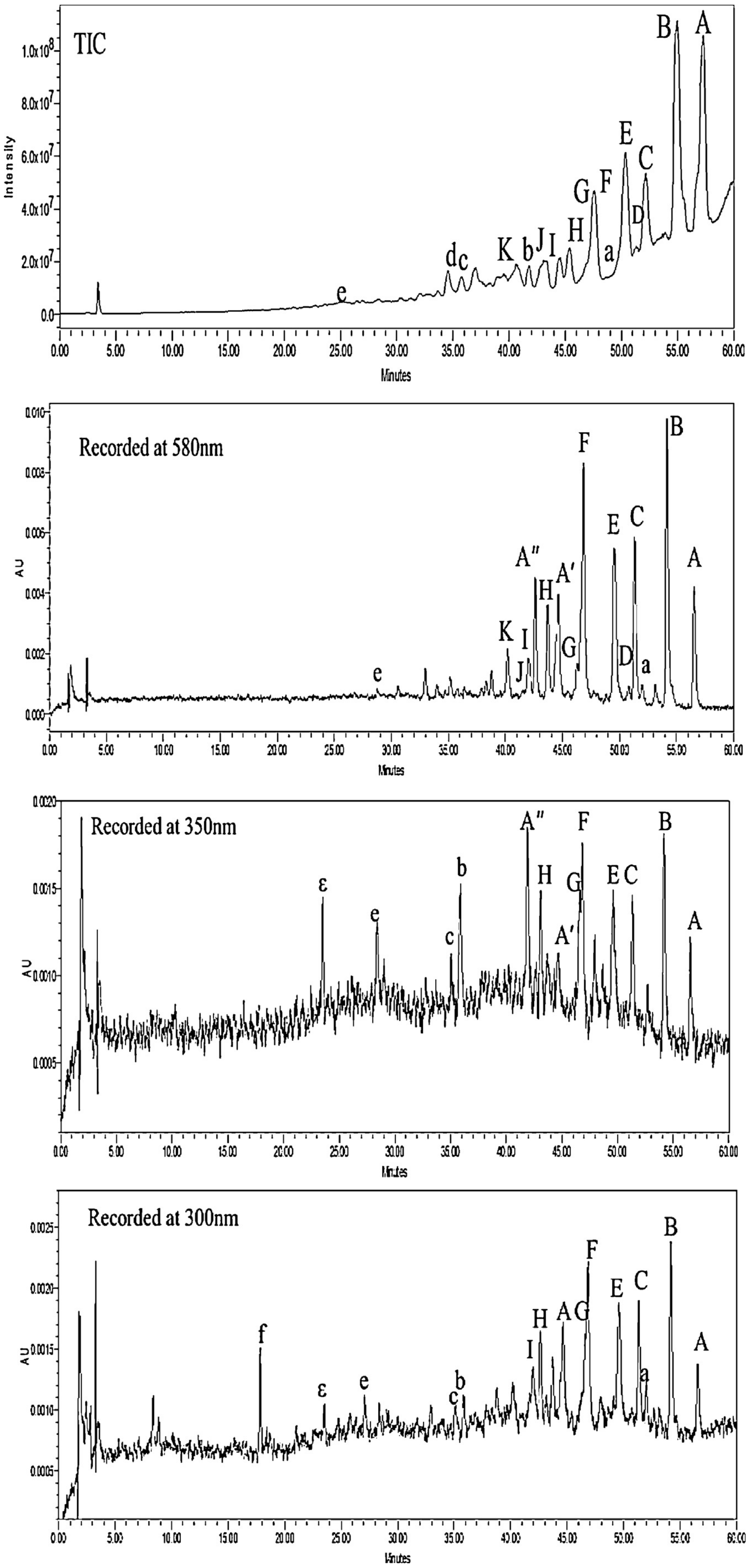

**Fig. 11.** Total ion chromatogram and HPLC chromatogram of the photocatalytic degradation intermediates with 24 h irradiation, recorded at 580 nm, 350 nm, and 300 nm.

**Table 3**
Identification of the intermediates from the photocatalytic degradation of VBR by HPLC–ESI-MS.

| TIC peaks | Intermediates | $[M+H^+]$ | Characteristic Absorption (nm) |
|---|---|---|---|
| A | Bis(4-dimethylaminophenyl)(4-ethylaminonaphthenyl)methylium | 422.2 | 619.2<br>561.6 |
| B | (4-Dimethylaminophenyl) (4-methylaminophenyl) (4-ethylaminonaphthyl)methylium | 408.2 | 609.4<br>561.6 |
| C | (4-Dimethylaminophenyl) (4-aminophenyl) (4-ethylaminonaphthyl)methylium | 394.2 | 600.8<br>554.3 |
| D | (4-Methylaminophenyl) (4-methylaminophenyl) (4-ethylaminonaphthyl)methylium | 394.3 | 598.0 |
| E | (4-Dimethylaminophenyl) (4-dimethylaminophenyl) (4-aminonaphthyl)methylium | 394.2 | 609.4<br>562.9 |
| F | (4-Methylaminophenyl) (4-aminophenyl) (4-ethylaminonaphthyl)methylium | 380.2 | 591.0 |
| G | (4-Dimethylaminophenyl) (4-methylaminophenyl) (4-aminonaphthyl)methylium | 380.2 | 605.7<br>591.0 |
| H | (4-Aminophenyl) (4-aminophenyl) (4-ethylaminonaphthyl)methylium | 366.2 | 589.8<br>563.3 |
| I | (4-Dimethylaminophenyl) (4-aminophenyl) (4-aminonaphthyl)methylium | 366.2 | 564.1 |
| J | (4-Methylaminophenyl) (4-methylaminophenyl) (4-aminonaphthyl)methylium | 366.3 | 560.4 |
| K | (4-Methylaminophenyl) (4-aminophenyl) (4-aminonaphthyl)methylium | 352.1 | 566.5 |
| A′ | (4-Hydroxymethylmethylaminophenyl)(4-dimethylmethylaminophenyl)(4-ethylaminonaphthyl)methylium | N/A | 598.3 |
| A″ | Bis(4-dimethylaminophenyl)(4-hydroxyethylaminonaphthyl)methylium | N/A | 592.2 |
| a | 4-(*N*,*N*-dimethylamino)-4′-(*N*′,*N*′-dimethylamino)benzophenone | 269.1 | 363.9<br>349.8 |
| b | 4-(*N*,*N*-dimethylamino)-4′-(*N*′-methylamino)benzophenone | 255.1 | 355.8 |
| c | 4-(*N*-methylamino)-4′-(*N*′-methylamino)benzophenone | 241.1 | 362.9 |
| d | 4-(*N*,*N*-dimethylamino)-4′-aminobenzophenone | 241.0 | 360.9 |
| e | 4-(*N*-methylamino)-4′-aminobenzophenone | 227.1 | 353.4 |

Wang et al. reported that the $^{\bullet}OH$ radical was generated by multistep reduction $O_2^{\bullet-}$ [44]. The generation of $O_2^{\bullet-}$ could not only inhibit the recombination of photoinduced charge carriers, but also benefit the dechlorination of chlorinated phenol derivative. Chen et al. reported that Pt–$TiO_2$ accumulated less negative species on catalyst surfaces, which deteriorated reaction rates, than pure $TiO_2$ in an acidic environment [45]. The $^{\bullet}OH$ radical is produced subsequently, as also shown in Eqs. (15)–(18):

$$O_2^{\bullet-} + H^+ + e^- \rightarrow HOO^{\bullet} \quad (15)$$

$$HOO^{\bullet} + H_2O \rightarrow {}^{\bullet}OH + H_2O_2 \quad (16)$$

$$O_2^{\bullet-} + 2H^+ \rightarrow H_2O_2 \quad (17)$$

$$H_2O_2 + e^- \rightarrow {}^{\bullet}OH + OH^- \quad (18)$$

These cycles continuously occur when the system is exposed to the UV light irradiation. Finally, after several cycles of photo-oxidation, the degradation of CV by the formed oxidant species can expressed by Eqs. (19) and (20):

$$CV + OH^{\bullet} \rightarrow \text{degraded compounds} \quad (19)$$

$$CV^{\bullet} + OH^{\bullet} \rightarrow \text{degraded compounds} \quad (20)$$

It has been reported that CV exhibits an mechanism of dye sensitized degradation [46,47]. This photocatalytic degradation is also attributed to the photodegradation of CV through the photocatalytic pathway of CV photosensitized β-$ZnMoO_4$. CV absorbing a visible photon is promoted to an excited electronic state $CV^*$, from which an electron can be transferred into the conduction band of β-$ZnMoO_4$:

$$CV + h\nu \rightarrow CV^* \quad (21)$$

$$CV^* + \beta\text{-}ZnMoO_4 \rightarrow CV^{+} + \beta\text{-}ZnMoO_4(e^-) \quad (22)$$

$$O_2 + e^- \rightarrow O_2^{\bullet-} \quad (23)$$

Once the electron reaches the β-$ZnMoO_4$ conduction band, it subsequently induces the generation of active oxygen species (Eqs. (23) and (15)–(18)), which result in the degradation of CV. Clearly, apart from the photodegradation of CV through the photocatalytic pathway of CV-photosensitized β-$ZnMoO_4$, there is another kind of photocatalytic pathway to account for the enhanced photocatalytic activity.

In earlier reports [45,48], the *N*-de-alkylation processes are preceded by the formation of a nitrogen-centered radical while oxidative degradation (destruction of dye chromophore structures) is preceded by the generation of a carbon-centered radical in the photocatalytic degradation of triphenylmethane dye. On the basis of all the above experimental results, we tentatively propose the dye degradation mechanism depicted in Fig. 12. The excited dye injects an electron into the conduction band of β-$ZnMoO_4$, where it is scavenged by $O_2$ to form $O_2^{\bullet-}$. De-alkylation of VBR dye occurs mostly through attack by the active species, which is a perfect nucleophilic reagent, on the *N*-alkyl portion of VBR. Further, $O_2^{\bullet-}$ subsequently reacts with $H_2O$ to generate $^{\bullet}OH$ radical and the other active radical. The probability for the formation of $^{\bullet}OH$ should be much lower than for that $O_2^{\bullet-}$. The $^{\bullet}OH$ is an extremely strong, non-selective oxidant, which leads to the partial or complete mineralization of several organic chemicals. All the above active radicals drive the photodegradation or mineralization of the dye molecule. Under UV or visible light irradiation, all the intermediates identified in these two studied topics have the same result. There is no doubt that the major oxidant is $^{\bullet}OH$ radical, not $O_2^{\bullet-}$.

During the initial period of VBR dye photodegradation by $ZnMoO_4$, competitive reactions between *N*-de-alkylation and oxidative degradation (cleavage of the VBR chromophore ring structure) occur based on the intermediates identified. The detailed mechanisms are illustrated in Fig. 12. The first pathway involves a hydroxyl radical attack on the *N*,*N*-alkylamino group of VBR, resulting in a reactive cationic radical, the subsequent de-alkylation and oxidation of which eventually yield the first groups intermediates. The results indicated that the *N*-de-

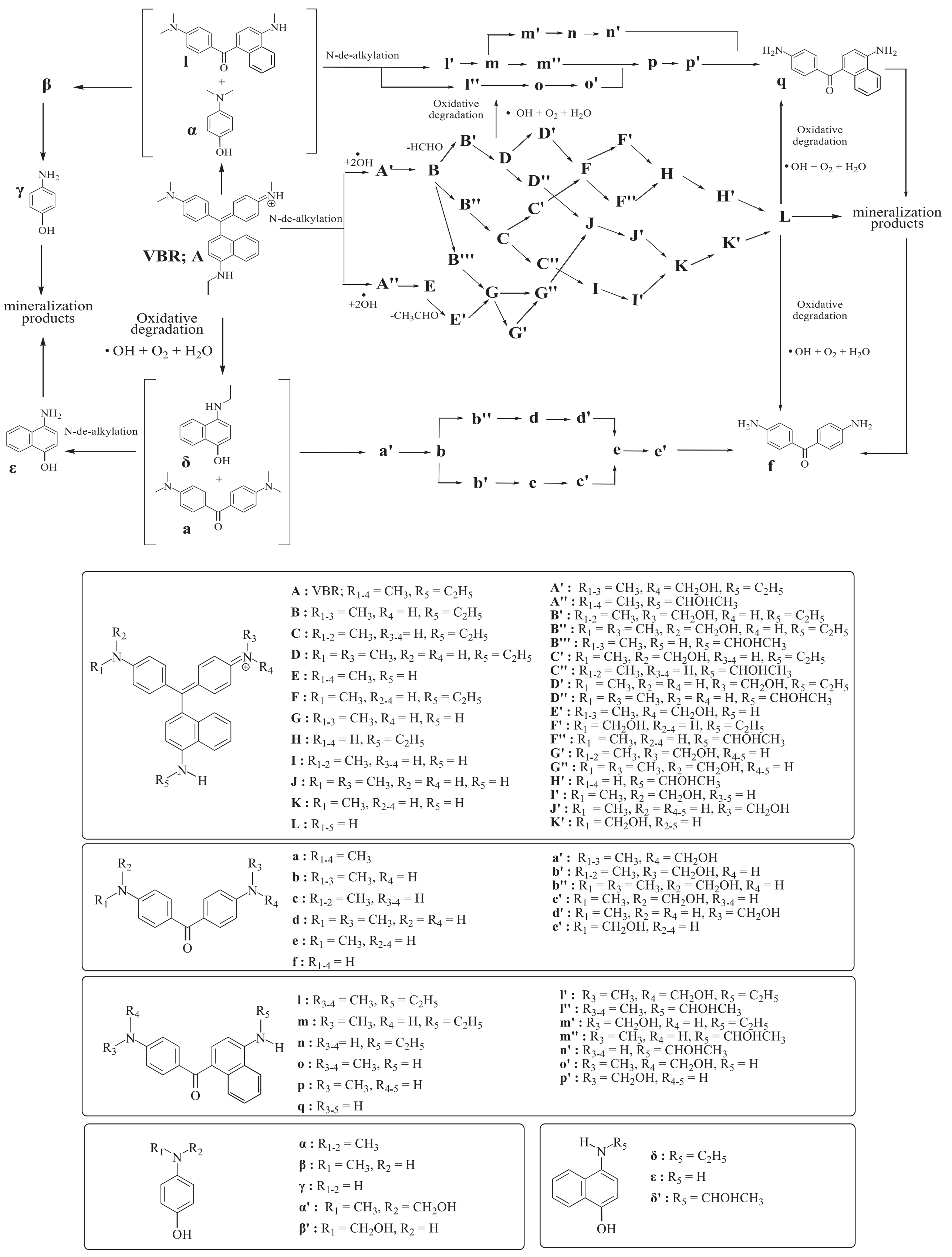

**Fig. 12.** Proposed mechanisms based on identification of intermediates formed chronologically during the photodegradation of VBR dye.

alkylation degradation of VBR dye took place in a stepwise manner to yield mono-, di-, tri-, tetra-, penta-, hexa- *N*-de-methylated and mono-*N*-de-ethylated VBR species during the process.

The second pathway involves a hydroxyl radical attack on the central carbon atom of VBR, yielding a reactive cationic radical, with a bond between the central carbon atom and the *N*,*N*-dimethylamino phenyl ring that is cleaved to give the two sets of intermediates $\alpha$ and l, and $\delta$ and a. In addition, these intermediates can further be attacked by hydroxyl radicals, giving a reactive cationic radical which is de-alkylated, resulting in $\gamma$, q, $\varepsilon$ and f. The latter intermediates are further oxidized to form mineralization products.

## 4. Conclusion

In summary, $\beta$-ZnMoO$_4$ crystals have been prepared using a conventional hydrothermal synthesis with a good control of the synthesis parameters. The obtained $\beta$-ZnMoO$_4$ is indirect transition semiconductors with optical band gap values of approximately 2.48–2.64 eV. The photocatalytic efficiencies of powder suspensions were evaluated by measuring the VBR and phenol concentration. The optical photocatalytic efficiencies for $\beta$-ZnMoO$_4$ photocatalysts with VBR are found to be hydrothermal treatment at 280 °C for 24 h under UV irradiation and at 230 °C for 12 h under visible light irradiation. This is the first study to reveal that excellent activities of $\beta$-ZnMoO$_4$ are a promising visible-light-responsive photocatalyst.

## Acknowledgement

This research was supported by the National Science Council of the Republic of China (NSC 99-2113-M-142-002-MY2).

## References

[1] Zhang G, Yu S, Yang Y, Jiang W, Zhang S, Huang B. Synthesis, morphology and phase transition of the zinc molybdates $ZnMoO_4\cdot 0.8H_2O/\alpha\text{-}ZnMoO_4/ZnMoO_4$ by hydrothermal method. J Cryst Growth 2010;312:1866–74.

[2] Cavalcante LS, Sczancoski JC, Siu Li M, Longo E, Varela JA. $\beta$-ZnMoO$_4$ microcrystals synthesized by the surfactant-assisted hydrothermal method: Growth process and photoluminescence properties. Colloid Surf A Physicochem Eng Aspects 2012;396:346–51.

[3] Xie A, Yuan X, Wang F, Shi Y, Mu Z. Enhanced red emission in $ZnMoO_4:Eu^{3+}$ by charge compensation. J Phys D Appl Phys 2010;43:55101.

[4] Ju X, Li X, Li W, Yang W, Tao C. Luminescence properties of $ZnMoO_4:Tb^{3+}$ green phosphor prepared via co-precipitation. Mater Lett 2011;65:2642–4.

[5] Burcham LJ, Briand LE, Wachs IE. Quantification of active sites for the determination of methanol oxidation turn-over frequencies using methanol chemisorption and in situ infrared techniques. 2. Bulk metal oxide catalysts. Langmuir 2001;17:6175–84.

[6] Zhou T, Hu J, Li J. $Er^{3+}$ doped bismuth molybdate nanosheets with exposed {0 1 0 0} facets and enhanced photocatalytic performance. Appl Catal B 2011;110:221–30.

[7] Zhou L, Wang W, Zhang L. Ultrasonic-assisted synthesis of visible-light-induced $Bi_2MO_6$ (M = W, Mo) photocatalysts. J Mol Catal A Chem 2007;268:195–200.

[8] Wang D, Zou Z, Ye J. A novel series of photocatalysts $M_{2.5}VMoO_8$ (M = Mg, Zn) for $O_2$ evolution under visible light irradiation. Catal Today 2004;93–95:891–4.

[9] Peng C, Gao L, Yang S, Sun J. A general precipitation strategy for large-scale synthesis of molybdate nanostructures. Chem Commun 2008;43:5601–3.

[10] Liao YHB, Wang JX, Lin JS, Chung WH, Lin WY, Chen CC. Synthesis, photocatalytic activities and degradation mechanism of $Bi_2WO_6$ toward crystal violet dye. Catal Today 2011;174:148–59.

[11] Fu H, Lin J, Zhang L, Zhu Y. Photocatalytic activities of a novel $ZnWO_4$ catalyst prepared by a hydrothermal process. Appl Catal A 2006;306:58–67.

[12] Edwin Suresh Raj AM, Mallika C, Swaminathan K, Sreedharan OM, Nagaraja KS. Zinc(II) oxide–zinc(II) molybdate composite humidity sensor. Sens Actuators B Chem 2002;81:229–36.

[13] Leyzerovich NN, Bramnik KG, Buhrmester T, Ehrenberg H, Fuess H. Electrochemical intercalation of lithium in ternary metal molybdates $MMoO_4$ (M: Cu, Zn, Ni and Fe). J Power Sources 2004;127:76–84.

[14] Spassky D, Vasil'ev A, Kamenskikh I, Kolobanov V, Mikhailin V, Savon A, et al. Luminescence investigation of zinc molybdate single crystals. Phys Stat Sol A 2009;206:1579–83.

[15] Amo BD, Romagnoli R, Vetere VF. Performance of zinc molybdenum phosphate in anticorrosive paints by accelerated and electrochemical tests. J Appl Electrochem 1999;29:1401–7.

[16] Wiley-VCH. Ullmann's encyclopedia of industrial chemistry. 6th ed. New York: John Wiley & Sons; 2002.

[17] Reichelt W, Weber T, Söhnel T, Däbritz S. Mischkristallbildung im system $CuMoO_4/ZnMoO_4$. Z Anorg Allg Chem 2000;626:2020–7.

[18] Pavani K, Ramanan A. Influence of 2-aminopyridine on the formation of molybdates under hydrothermal conditions. Eur J Inorg Chem 2005;15:3080–7.

[19] Sczancoski JC, Bomio MDR, Cavalcante LS, Joya MR, Pizani PS, Varela JA, et al. Morphology and blue photoluminescence emission of $PbMoO_4$ processed in conventional hydrothermal. J Phys Chem C 2009;113:5812–22.

[20] Longo VM, Gracia L, Stroppa DG, Cavalcante LS, Orlandi M, Ramirez AJ, et al. A joint experimental and theoretical study on the nanomorphology of $CaWO_4$ crystals. J Phys Chem C 2011;115:20113–19.

[21] Lin WC, Yang WD, Jheng SY. Photocatalytic degradation of dyes in water using porous nanocrystalline titanium dioxide. J Taiwan Inst Chem Eng 2012;43:269–74.

[22] Lv L, Tong W, Zhang Y, Su Y, Wang X. Metastable monoclinic $ZnMoO_4$: hydrothermal synthesis, optical properties and photocatalytic performance. J Nanosci Nanotechnol 2012;11:9506–12.

[23] Shen TFR, Lai MH, Yang TCK, Fu IP, Liang NY, Chen WT. Photocatalytic production of hydrogen by vanadium oxides under visible light irradiation. J Taiwan Inst Chem Eng 2012;43:95–101.

[24] Lei F, Yan B, Chen H-H, Zhang Q, Zhao JT. Surfactant-assisted hydrothermal synthesis, physical characterization, and photoluminescence of $PbWO_4$. Cryst Growth Des 2009;9:3730–6.

[25] Yan X, Cui Y, Qi W, Su Y, Yang Y, He Q, et al. Self-assembly of peptide-based colloids containing lipophilic nanocrystals. Small 2008;4:1687–93.

[26] Bayati MR, Golestani-Fard F, Moshfegh AZ. Visible photodecomposition of methylene blue over micro arc oxidized $WO_3$-loaded $TiO_2$ nano-porous layers. Appl Catal A 2010;382:322–31.

[27] Malik PK. Use of activated carbons prepared from sawdust and rice-husk for adsorption of acid dyes: a case study of Acid Yellow 36. Dyes Pigment 2003;56:239–49.

[28] Kim M-J, Huh Y-D. Ligand-assisted hydrothermal synthesis of $ZnWO_4$ rods and their photocatalytic activities. Mater Res Bull 2010;45:1921–4.

[29] Ryu JH, Koo S-M, Yoon J-W, Lim CS, Shim KB. Synthesis of nanocrystalline $MMoO_4$ (M = Ni, Zn) phosphors via a citrate complex route assisted by microwave irradiation and their photoluminescence. Mater Lett 2006;60:1702–5.

[30] Cavalcante LS, Sczancoski JC, Tranquilin RL, Varela JA, Longo E, Orlandi MO. Growth mechanism of octahedron-like $BaMoO_4$ microcrystals processed in microwave-hydrothermal: experimental observations and computational modeling. Particuology 2009;7:353–62.

[31] Li XZ, Walker B, Michaelides A. Quantum nature of the hydrogen bond. PNAS 2011;108:6369–73.

[32] Tian Y, Chen B, Yu H, Hua R, Li X, Sun J, et al. Controllable synthesis and luminescent properties of three-dimensional nanostructured $CaWO_4:Tb^{3+}$ microspheres. J Colloid Interface Sci 2011;360:586–92.

[33] Mi Y, Huang Z, Hu F, Li Y, Jiang J. Room-temperature synthesis and luminescent properties of single-crystalline $SrMoO_4$ nanoplates. J Phys Chem C 2009;113:20795–99.

[34] Moreira ML, Andrés J, Mastelaro VR, Varela JA, Longo E. On the reversed crystal growth of $BaZrO_3$ decaoctahedron: shape evolution and mechanism. CrystEngComm 2011;13:5818–24.

[35] Bhattacharya S, Kar T, Bar A, Arun KR, Roy D, Graca MPF, Valente MA. Structural behaviors and optical properties of semiconducting zinc–molybdate glass nanocomposites. Sci Adv Mater 2011;3:284–8.

[36] Keereeta Y, Thongtem T, Thongtem S. Characterization of $ZnMoO_4$ nanofibers synthesized by electrospinning–calcination combinations. Mater Lett 2012;68:265–8.

[37] Spassky DA, Vasil'ev AN, Kamenskikh IA, Mikhailin VV, Savon AE, Hizhnyi YA, et al. Electronic structure and luminescence mechanisms in $ZnMoO_4$ crystals. J Phys 2011;23:365501–510.

[38] Lu C, Wu Y, Mai F, Chung W, Wu C, Lin W, et al. Degradation efficiencies and mechanisms of the ZnO-mediated photocatalytic degradation of Basic Blue 11 under visible light irradiation. J Mol Catal A Chem 2009;310:159–65.

[39] Cavalcante LS, Sczancoski JC, Batista NC, Longo E, Varela JA, Orlandi MO. Growth mechanism and photocatalytic properties of $SrWO_4$ microcrystals synthesized by injection of ions into a hot aqueous solution. Adv Powder Technol 2013;24:344–53.

[40] Cavalcante LS, Batista FMC, Almeida MAP, Rabelo AC, Nogueira IC, Batista NC, et al. Structural refinement, growth process, photoluminescence and photocatalytic properties of $(Ba_{1-x}Pr_{2x/3})WO_4$ crystals synthesized by the coprecipitation method. RSC Adv 2012;2:6438–54.

[41] Montini T, Gombac V, Hameed A, Felisari L, Adami G, Fornasiero P. Synthesis, characterization and photocatalytic performance of transition metal tungstates. Chem Phys Lett 2010;498:113–9.

[42] Rajeshwar K, Osugi ME, Chanmanee W, Chenthamarakshan CR, Zanoni MVB, Kajitvichyanukul P, et al. Heterogeneous photocatalytic treatment of organic dyes in air and aqueous media. J Photochem Photobiol C 2008;9:171–92.

[43] Yu K, Yang S, He H, Sun C, Gu C, Ju Y. Visible light-driven photocatalytic degradation of rhodamine B over $NaBiO_3$: pathways and mechanism. J Phys Chem A 2009;113:10024–32.

[44] Wang J, Yu Y, Zhang L. Highly efficient photocatalytic removal of sodium pentachlorophenate with $Bi_3O_4Br$ under visible light. Appl Catal B Environ 2013;136-137:112–21.

[45] Fan HJ, Lu CS, Lee WLW, Chiou MR, Chen CC. Mechanistic pathways differences between P25–$TiO_2$ and Pt–$TiO_2$ mediated CV photodegradation. J Hazard Mater 2011;185:227–35.

[46] Li Y, Zhang H, Hu X, Zhao X, Han M. Efficient visible-light-induced photocatalytic activity of a 3D-ordered titania hybrid photocatalyst with a core/shell structure of dye-containing polymer/titania. J Phys Chem C 2008;112:14973–79.

[47] Wu T, Liu G, Zhao J, Hidaka H, Serpone N. Evidence for $H_2O_2$ generation during the $TiO_2$-assisted photodegradation of dyes in aqueous dispersions under visible light illumination. J Phys Chem B 1999;103:4862–7.

[48] Lee WLW, Huang ST, Chang JL, Chen JY, Cheng MC, Chen CC. Photodegradation of CV over nanocrystalline bismuth tungstate prepared by hydrothermal synthesis. J Mol Catal A Chem 2012;361–362:80–90.